

GHOST Commissioning Science Results II: a very metal-poor star witnessing the early Galactic assembly

Federico Sestito^{1*}, Christian R. Hayes², Kim A. Venn¹, Jaclyn Jensen¹, Alan W. McConnachie^{2,1}, John Pazder^{2,1}, Fletcher Waller¹, Anke Arentsen³, Pascale Jablonka^{4,5}, Nicolas F. Martin^{6,7}, Tadafumi Matsuno⁸, Julio F. Navarro¹, Else Starkenburg⁸, Sara Vitali⁹, John Bassett¹⁰, Ruben Diaz¹⁰, Michael L. Edgar¹¹, Veronica Firpo¹⁰, Manuel Gomez-Jimenez¹⁰, Venu Kalari¹⁰, Sam Lambert², Jon Lawrence¹², Gordon Robertson¹², Roque Ruiz-Carmona¹⁰, Ricardo Salinas¹⁰, Kim M. Sebo¹³, and Sudharshan Venkatesan¹²

¹ Department of Physics and Astronomy, University of Victoria, PO Box 3055, STN CSC, Victoria BC V8W 3P6, Canada

² NRC Herzberg Astronomy & Astrophysics, 5071 West Saanich Road, Victoria, BC V9E 2E7, Canada

³ Institute of Astronomy, University of Cambridge, Madingley Road, Cambridge CB3 0HA, UK

⁴ Laboratoire d'astrophysique, École Polytechnique Fédérale de Lausanne (EPFL), Observatoire, CH-1290 Versoix, Switzerland

⁵ GEPI, Observatoire de Paris, Université PSL, CNRS, 5 Place Jules Janssen, F-92195 Meudon, France

⁶ Université de Strasbourg, CNRS, Observatoire astronomique de Strasbourg, UMR 7550, F-67000 Strasbourg, France

⁷ Max-Planck-Institut für Astronomie, Königstuhl 17, D-69117 Heidelberg, Germany

⁸ Kapteyn Astronomical Institute, University of Groningen, Landleven 12, NL-9747AD Groningen, the Netherlands

⁹ Instituto de Estudios Astrofísicos, Facultad de Ingeniería y Ciencias, Universidad Diego Portales, Av. Ejército Libertador 441, Santiago, Chile

¹⁰ Gemini Observatory/NSF's NOIRLab, Casilla 603, La Serena, Chile

¹¹ Australian Astronomical Observatory

¹² Australian Astronomical Optics, Macquarie University, 105 Delhi Rd, North Ryde NSW 2113, Australia

¹³ Research School of Astronomy and Astrophysics, College of Science, Australian National University, Canberra 2611, Australia

Accepted XXX. Received YYY; in original form ZZZ

ABSTRACT

This study focuses on Pristine_180956.78–294759.8 (hereafter P180956, $[\text{Fe}/\text{H}] = -1.95 \pm 0.02$), a star selected from the Pristine Inner Galaxy Survey (PIGS), and followed-up with the recently commissioned Gemini High-resolution Optical SpecTrograph (GHOST) at the Gemini South telescope. The GHOST spectrograph's high efficiency in the blue spectral region (3700 – 4800 Å) enables the detection of elemental tracers of early supernovae (e.g., Al, Mn, Sr, Eu), which were not accessible in the previous analysis of P180956. The star exhibits chemical signatures resembling those found in ultra-faint dwarf systems, characterised by very low abundances of neutron-capture elements (Sr, Ba, Eu), which are uncommon among stars of comparable metallicity in the Milky Way. Our analysis suggests that P180956 bears the chemical imprints of a small number (2 or 4) of low-mass hypernovae ($\sim 10 - 15 M_{\odot}$), which are needed to reproduce the abundance pattern of the light-elements (e.g., $[\text{Si}, \text{Ti}/\text{Mg}, \text{Ca}] \sim 0.6$), and one fast-rotating intermediate-mass supernova ($\sim 300 \text{ km s}^{-1}$, $\sim 80 - 120 M_{\odot}$). Both types of supernovae explain the high $[\text{Sr}/\text{Ba}]$ of P180956 (~ 1.2). The small pericentric ($\sim 0.7 \text{ kpc}$) and apocentric ($\sim 13 \text{ kpc}$) distances and its orbit confined to the plane ($\lesssim 2 \text{ kpc}$), indicate that this star was likely accreted during the early Galactic assembly phase. Its chemo-dynamical properties suggest that P180956 formed in a system similar to an ultra-faint dwarf galaxy accreted either alone, as one of the low-mass building blocks of the proto-Galaxy, or as a satellite of Gaia-Sausage-Enceladus. The combination of Gemini's large aperture with GHOST's high efficiency and broad spectral coverage makes this new spectrograph one of the leading instruments for near-field cosmology investigations.

Key words: Galaxy: formation - Galaxy: evolution - Galaxy: bulge - Galaxy: abundances - stars: kinematics and dynamics - stars: Population II

1 INTRODUCTION

Low-metallicity stars are among the oldest stars in the Galaxy. Cosmological simulations suggest that most metal-

poor stars formed within 2–3 Gyr after the Big Bang, likely in low-mass systems that were accreted early on into the Galaxy ("building blocks", e.g., Starkenburg et al. 2017a; El-Badry et al. 2018; Sestito et al. 2021). These merging building blocks contributed stars, gas, and dark matter to the proto-Milky Way. Because they formed at the bottom of

* Email: sestitof@uvic.ca

the potential well of the merging building blocks, these stars are predicted to occupy the inner regions of the present-day Galaxy (e.g., [White & Springel 2000](#); [Starkenburg et al. 2017a](#); [El-Badry et al. 2018](#); [Sestito et al. 2021](#)). Systems accreted later are anticipated to disperse their stars primarily in the halo ([Bullock & Johnston 2005](#); [Johnston et al. 2008](#); [Tissera et al. 2012](#)), or possibly the disc (e.g., [Abadi et al. 2003](#); [Sestito et al. 2021](#); [Santistevan et al. 2021](#)). An in-situ component may also form from the gas deposited by the building blocks, recently called the Aurora stars ([Belokurov & Kravtsov 2022](#)). This in-situ component may have formed in a lumpy and chaotic interstellar medium (ISM), possibly resembling the chemical properties of globular clusters ([Belokurov & Kravtsov 2023](#)).

The most chemically pristine stars in the Milky Way (MW) may have been enriched by only one or a few supernovae or hypernovae events (e.g., [Frebel et al. 2010a](#); [Ishigaki et al. 2018](#)). The study of the orbital properties and chemical abundance patterns of pristine stars is essential for understanding the lives and deaths of the first stars and the assembly history of the Galaxy (e.g., [Freeman & Bland-Hawthorn 2002](#); [Venn et al. 2004](#); [Tumlinson 2010](#); [Wise et al. 2012](#); [Karlsson et al. 2013](#)).

Metal-poor stars in and towards the Galactic bulge can serve as important tracers of the earliest stages of Galactic assembly, yet their detection is extremely challenging (e.g., [Schlaufman & Casey 2014](#); [Lamb et al. 2017](#)). The inner regions of the MW are dominated by a metal-rich population and disrupted globular clusters ([Ness et al. 2013a, 2014](#); [Bensby et al. 2013, 2017](#); [Schiavon et al. 2017](#); [Schultheis et al. 2019](#)). Furthermore, extreme interstellar extinction and stellar crowding have made photometric surveys of bulge metal-poor stars exceedingly difficult.

The Abundances and Radial velocity Galactic Origins Survey (ARGOS, [Ness et al. 2013b](#)) found that $\lesssim 1$ percent of their sample had $[\text{Fe}/\text{H}]^1 < -1.5$, resulting in a total of 84 stars. The metallicity-sensitive photometric filter from the SkyMapper Southern Survey ([Bessell et al. 2011](#); [Wolf et al. 2018](#)) has been used by the Extremely Metal-poor BuLge stars with AAOmega (EMBLA, [Howes et al. 2014, 2015, 2016](#)) survey to select very metal-poor stars (VMPs, $[\text{Fe}/\text{H}] \leq -2.0$). Their high-resolution analysis of 63 VMPs revealed that the majority resembled chemically metal-poor stars in the Galactic halo, with the exception of a lack of carbon-rich stars and a larger scatter in $[\alpha/\text{Fe}]$ abundances. Additionally, their kinematic analysis found that it was challenging to distinguish stars that were born in the bulge from those that are merely in the inner halo. The Chemical Origins of Metal-poor Bulge Stars (COMBS, [Lucey et al. 2019](#)) studied the chemo-dynamical properties of inner Galactic stars, finding that around ~ 50 percent of their sample is composed of halo interlopers, while their chemical properties resemble those of the halo ([Lucey et al. 2021, 2022](#)).

Similar to the EMBLA survey, the Pristine Inner Galaxy Survey (PIGS, [Arentsen et al. 2020a,b](#)) selected metal-poor targets from the narrow-band photometry of the Pristine survey ([Starkenburg et al. 2017b](#)). The Pristine survey, conducted at the Canada-France-Hawaii Tele-

scope (CFHT), utilises the CaHK filter in combination with broad-band photometry to provide a highly efficient method of identifying low-metallicity stars (~ 56 percent success rate at $[\text{Fe}/\text{H}] \leq -2.5$, [Youakim et al. 2017](#); [Aguado et al. 2019](#); [Venn et al. 2020](#); [Lucchesi et al. 2022](#)). Around $\sim 12,000$ inner Galaxy metal-poor candidates selected by PIGS were observed with low-/medium-resolution spectroscopy using the AAOmega spectrograph on the Anglo Australian Telescope (AAT). The results of these observations showed ~ 80 percent efficiency in identifying VMP stars towards the bulge ([Arentsen et al. 2020b](#)) and the Sagittarius dwarf galaxy ([Vitali et al. 2022](#)) using the Pristine metallicity-sensitive filter for initial selection. Interestingly, within PIGS, [Mashonkina et al. \(2023\)](#) reports the serendipitous discovery of the first r- and s- processes rich Carbon-enhanced star (CEMP-r/s) in the inner Galaxy.

In a recent study, [Sestito et al. \(2023b\)](#) analysed high-resolution spectra of 17 metal-poor stars selected from the PIGS survey taken with the Gemini Remote Access to CFHT ESPaDOnS Spectrograph (GRACES, [Chene et al. 2014](#); [Pazder et al. 2014](#)). Their findings, consistent with [Howes et al. \(2016\)](#), indicate that the chemo-dynamical properties of the VMP population in the inner Galaxy resemble that of the halo, suggesting a common origin from disrupted building blocks. [Sestito et al. \(2023b\)](#) report stars with chemical abundances compatible with those of disrupted second-generation globular clusters (GC), one with exceptionally low metallicity ($[\text{Fe}/\text{H}] \sim -3.3$), well below the metallicity floor of GCs ($[\text{Fe}/\text{H}] \sim -2.8$, [Beasley et al. 2019](#)). This provides further evidence that extremely metal-poor structures (EMPs, $[\text{Fe}/\text{H}] \leq -3.0$) can form in the early Universe (see also [Martin et al. 2022](#), on the discovery of the disrupted EMP globular cluster, C-19).

In this paper, we present a new analysis of the inner Galactic very metal-poor Pristine_180956.78–294759.8 (P180956), from spectra taken during the commissioning of the new Gemini High-resolution Optical SpecTrograph (GHOST, [Pazder et al. 2020](#)). This star was previously analysed in the PIGS/GRACES analysis ([Sestito et al. 2023b](#)), but it can be observed from either the northern hemisphere (GRACES) or the south (GHOST, at Gemini South). P180956 is selected for this work for its unusually low $[\text{Na}, \text{Ca}/\text{Mg}]$ and $[\text{Ba}/\text{Fe}]$ ratios and for its high eccentric orbit that remains confined close to the Milky Way plane. The new GHOST spectrograph has also been used in the analysis of two stars in the Reticulum II ultra-faint dwarf galaxy ([Hayes et al. 2023](#)), and the presentation of the spectrum of the r-process rich standard star HD 222925 ([Hayes et al. 2022](#); [McConnachie et al. 2022](#)). GHOST’s wide spectral coverage and its high efficiency in the blue region are crucial to detect species that are tracers of the early chemical evolution (e.g., Al, Mn, Sr, Eu) and that were not accessible with GRACES spectrograph.

The instrument setup and data reduction are described in Section 2. Sections 3 and 4 discuss the model atmospheres analysis and the chemical abundance analyses, respectively. Orbital parameters are reported in Section 5. The results are discussed in Section 6, focusing on the type of supernovae that polluted the formation site of P180956, and its origin in an ancient dwarf system, which may have resembled today’s ultra-faint dwarfs. Conclusions are presented in Section 7.

¹ $[\text{Fe}/\text{H}] = \log(N_{\text{Fe}}/N_{\text{H}})_{\star} - \log(N_{\text{Fe}}/N_{\text{H}})_{\odot}$, where N_X represents the number density of element X.

2 DATA

2.1 GHOST observations

The target (G = 13.50 mag), P180956, was initially observed as part of the PIGS photometric survey using MegaCam at the Canada-France-Hawaii Telescope (CFHT). Its small pericentric distance ($r_{\text{peri}} \sim 0.7$ kpc), the apocentre (~ 13 kpc), the limited maximum excursion from the plane ($Z_{\text{max}} \sim 1.8$ kpc), and its high eccentricity ($e \sim 0.90$) imply that it was likely accreted during the early stages of Galactic assembly (Sestito et al. 2023b). A low/medium-resolution ($R \sim 1,300$ and $R \sim 11,000$) spectrum of P180956 was obtained using AAT/AAOmega (Arentsen et al. 2020b), and also with the Gemini Remote Access to CFHT ESPaDOnS Spectrograph (GRACES, $R \sim 40,000$, Chene et al. 2014; Pazder et al. 2014) as part of LLP-102 (PI K.A. Venn). The GRACES spectrum was analysed by Sestito et al. (2023b) along with 16 other VMP stars in the Galactic bulge; however, due to limitations in the throughput of the 300-metre optical fiber, the bluest spectral regions were not accessible for that study. The GRACES spectral analysis was limited to a range of 4900–10000 Å only. Thus, P180956 was chosen as a commissioning target for the Gemini High-resolution Optical SpecTrograph (GHOST, Pazder et al. 2020). The instrument’s high efficiency in the blue spectral region makes it ideal for detecting spectral features of additional chemical elements which allow a deeper investigation of the origins of P180956.

The target was observed on September 12th, 2022, during the second commissioning run of GHOST. Three acquisitions, each lasting 600 seconds, were conducted. The instrument was configured in the standard resolution ($R \sim 50,000$) single object mode, employing a spectral and spatial binning of 2 and 4, respectively. This specific setup and exposure times were chosen to enable the detection of spectral lines from species in the bluer regions (~ 4000 Å) of the spectrum that were not accessible with GRACES, i.e., C, Al, Si, Sc, V, Mn, Co, Cu, Zn, Sr, Y, La, Eu. Table 1 reports the *Gaia* DR3 source ID and photometry, the reddening from Green et al. (2019) along with the total exposure time and the number of exposures.

2.2 Data reduction

The acquired spectra were processed using the GHOST Data Reduction pipeline (GHOSTDR, Ireland et al. 2018; Hayes et al. 2022), which is integrated into the DRAGONS suite (Labrie et al. 2019). This pipeline² generates 1D spectra for the blue and red arms, which were wavelength calibrated, order-combined, and sky-subtracted. Subsequently, the spectra were individually normalized through polynomial fitting, and barycentric corrections were applied. A radial velocity correction was performed using the DOPPLER code³, employing a VMP template synthesized with TURBOSPECTRUM⁴ (Plez 2012) and a MARCS⁵ model atmosphere (Gustafsson et al. 2008). The radial velocity mea-

sured from the blue arm is $RV = 263.034 \pm 0.020$ km s^{−1}, while from the red arm is $RV = 262.918 \pm 0.362$ km s^{−1}. Their average, $RV = 262.976 \pm 0.363$ km s^{−1}, is in agreement by 0.8σ with the measurement from the GRACES analysis ($RV = 262.45 \pm 0.54$ km s^{−1}, Sestito et al. 2023b) and by 2.3σ with the value from the low-/medium-resolution PIGS campaign ($RV = 264.86 \pm 0.73$ km s^{−1}, Arentsen et al. 2020a). The lack of RV variation likely rules out the possibility that the object is in a binary system. The continuum points in the observations were identified using spectral templates and fitted via an iterative sigma clipping method to obtain a normalised spectrum. Finally, the blue and red output spectra were merged, taking into account the signal-to-noise ratio (SNR) in the overlapping regions.

Figure 1 showcases the reduced spectrum of P180956. In the top panel, a comparison is made with the GRACES observation in the 4400–5200 Å region. Both instruments have similar spectral (high) resolution; however, the SNR of the GRACES spectrum (black line) deteriorates below 5000 Å, a region where the number of spectral lines clearly increases, as seen in the GHOST spectrum (blue). The Balmer line H- ϵ , the Ca II H&K lines, along with two Al I lines, two Ti I, five Fe I lines, and one Co I line are shown in the central panel. The Mg Ib Triplet region also contains several Fe and Ti lines, as shown in the bottom panel. Table 1 reports the SNR measured close to the Eu II 4129 Å line, the Mg Ib Triplet region, and to the Na I Doublet.

3 MODEL ATMOSPHERES ANALYSIS

3.1 Stellar parameters

The stellar parameters used in this study are adopted from the GRACES analysis by Sestito et al. (2023b), $T_{\text{eff}} = 5391 \pm 133$ K, $\log g = 1.87 \pm 0.10$. To briefly summarize, the effective temperature is estimated based on the color-temperature relationship derived by Mucciarelli et al. (2021). This relationship is based on the Infrared Flux Method introduced by González Hernández & Bonifacio (2009) and adapted to the *Gaia* EDR3 photometry. The surface gravity is determined by applying the Stefan-Boltzmann equation, inferred assuming a flat mass distribution between 0.5 to 0.8 M_{\odot} . These calculations rely on several factors: 1) the de-reddened photometry⁶; 2) the distance to the star, which is estimated to be 3.30 ± 0.27 kpc (Sestito et al. 2023b); and 3) a metallicity (taken as $[\text{Fe}/\text{H}] = -2.0 \pm 0.1$, Sestito et al. 2023b). Uncertainties on the stellar parameters are derived using a Monte Carlo simulation.

A first estimate of the microturbulence velocity (v_{micro}) was calculated using the relation provided by Mashonkina et al. (2017a). However, that value was slightly revised to 1.5 km s^{−1} to achieve a flatter distribution in the abundances from the Fe I lines, $A(\text{Fe I})$ vs. the reduced equivalent width.

⁶ Extinction is from the 3D map of Green et al. (2019). To convert from the E(B-V) map to *Gaia* extinction coefficients, the $A_V/E(B-V) = 3.1$ (Schultz & Wiemer 1975) and the $A_G/A_V = 0.85926$, $A_{BP}/A_V = 1.06794$, $A_{RP}/A_V = 0.65199$ relations (Marigo et al. 2008; Evans et al. 2018) are used.

² <https://github.com/GeminiDRSoftware/GHOSTDR>

³ <https://github.com/dnidever/doppler>

⁴ <https://github.com/bertrandplez/Turbospectrum2019>

⁵ <https://marcs.astro.uu.se>

Table 1. Log of the observations. The Pristine name, the short name, the source ID, G, and BP–RP from *Gaia* DR3, the reddening from the 3D map of [Green et al. \(2019\)](#), the total exposure time, the number of exposures, the SNR, and the radial velocity are reported. The SNR is measured as the ratio between the median flux and its standard deviation in three spectral regions, close to the Eu II 4129 Å, in the Mg Ib Triplet and in the Na I Doublet.

Pristine name	source ID	G (mag)	BP–RP (mag)	E(B–V) (mag)	T _{exp} (s)	N _{exp}	SNR @Eu II, @Mg Ib, @Na I	RV (km s ^{−1})
Pristine_180956.78–294759.8	4050071013878221696	13.50	1.55	0.53	1800	3	16, 50, 65	262.976 ± 0.363

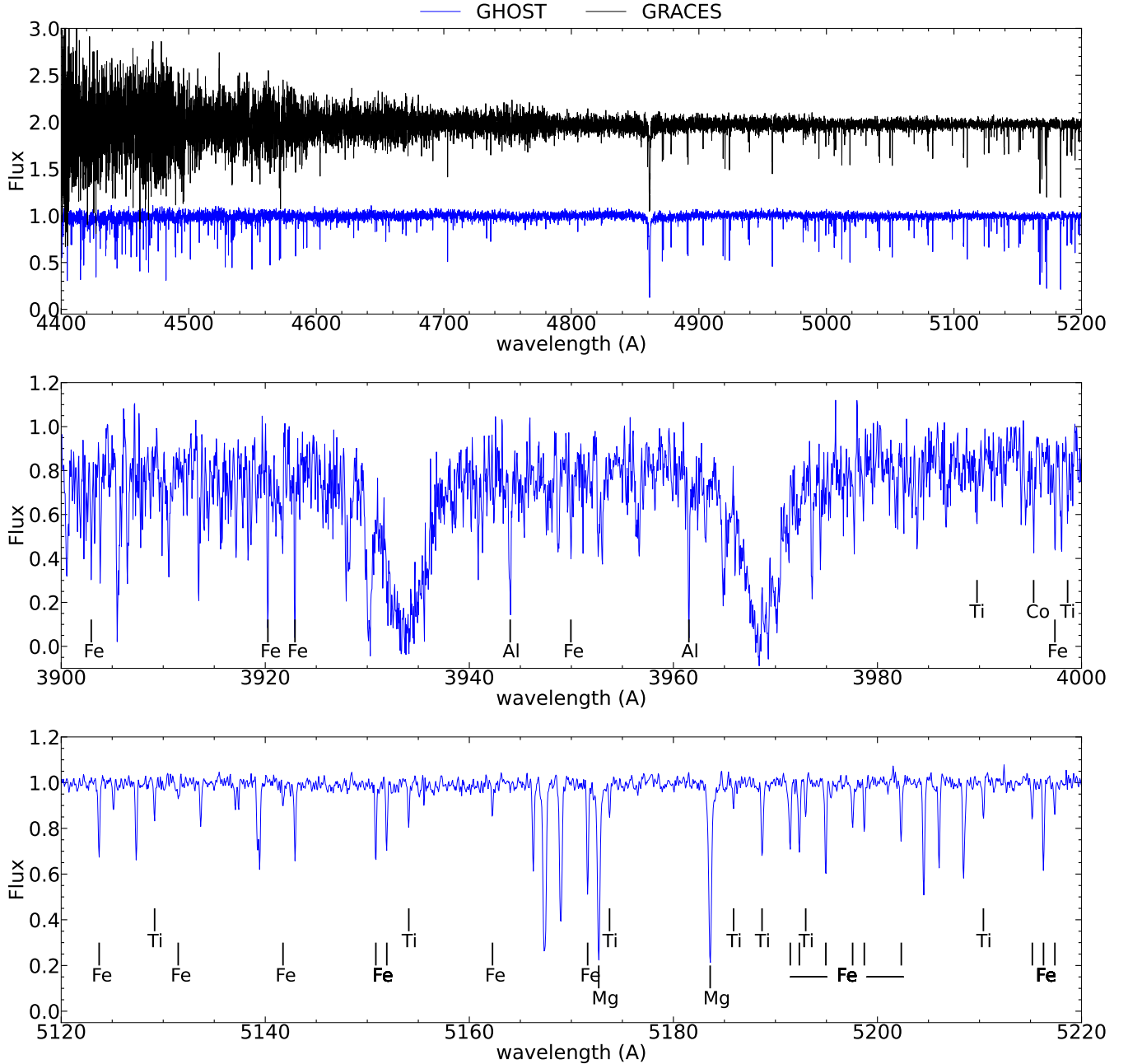


Figure 1. GHOST spectrum of P180956. Top panel: Wide spectral region, 4400 – 5200 Å, also showing the GRACES spectrum (black line). Central panel: blue region 3900 – 4000 Å. Bottom panel: Mg Ib Triplet. Spectral lines used for the chemical abundance analysis are marked.

3.2 Spectral lines and atomic data

The spectral line list is generated with LINEMAKE (Placco et al. 2021), including lines with hyper-fine structure corrections (Sc, V, Mn, Co, and Cu), molecular bands (CH in the 4300 Å region), and isotopic corrections (Sr, Ba, Eu).

An initial measurement of the equivalent width is performed using DAOSPEC (Stetson & Pancino 2008), which automatically fits Gaussian profiles to spectra following the input line list. Given the signal-to-noise ratio of our spectrum, lines weaker than 15 mÅ are rejected, and lines stronger than 100 mÅ are further examined with non-Gaussian measurements. The equivalent widths are then used with the MOOG⁷ spectrum synthesis code (Snedden 1973; Sobek et al. 2011) to determine the chemical abundances assuming Local Thermodynamic Equilibrium (LTE). The spherical MARCS⁸ model atmospheres (Gustafsson et al. 2008; Plez 2012) are used for the chemical abundance analysis in this paper, which yield to $[\text{Fe}/\text{H}] = -1.95 \pm 0.02$. The chemical abundances of Sc, Cu, Y, Ba, La, and Eu are determined using the SYNTH mode within MOOG.

The list of spectral lines used for the chemical abundance analysis, their EWs or abundances from synthesis are reported as supplementary online material.

3.3 Uncertainties on the chemical abundances

MOOG provides estimates of the chemical abundances $A(X)$ along with their line-to-line scatter, $\delta_{A(X)}$. The total abundance uncertainties in this paper are calculated by combining the line-to-line scatter (δ_{EW}) with the uncertainties resulting from variations in the stellar parameters ($\delta_{T_{\text{eff}}}$, $\delta_{\log g}$), in quadrature. The final uncertainty for element X is given by $\sigma_{A(X)} = \delta_{A(X)} / \sqrt{N_X}$. In case there is only one spectral line or SYNTH mode is employed, the dispersion in Fe I lines is considered as the typical dispersion.

4 CHEMICAL ABUNDANCE ANALYSIS

The blue wavelength coverage of GHOST permits an analysis of the spectral lines of many elements in metal-poor stars, including a range of α -, odd-Z, Fe-peak, and neutron-capture process elements.

4.1 Carbon

Carbon was first inferred from the low-/medium-resolution campaign of PIGS (Arentsen et al. 2020a), showing the star is Carbon-normal, $[\text{C}/\text{Fe}] = 0.17 \pm 0.24$. Figure 2 shows the synthesis on the CH bands in the 4300 Å region (top panel) and the residuals (bottom panel). The synthesis is made with SYNTH mode of MOOG, yielding a $[\text{C}/\text{Fe}] = 0.2 \pm 0.1$, in agreement with the previous measurement.

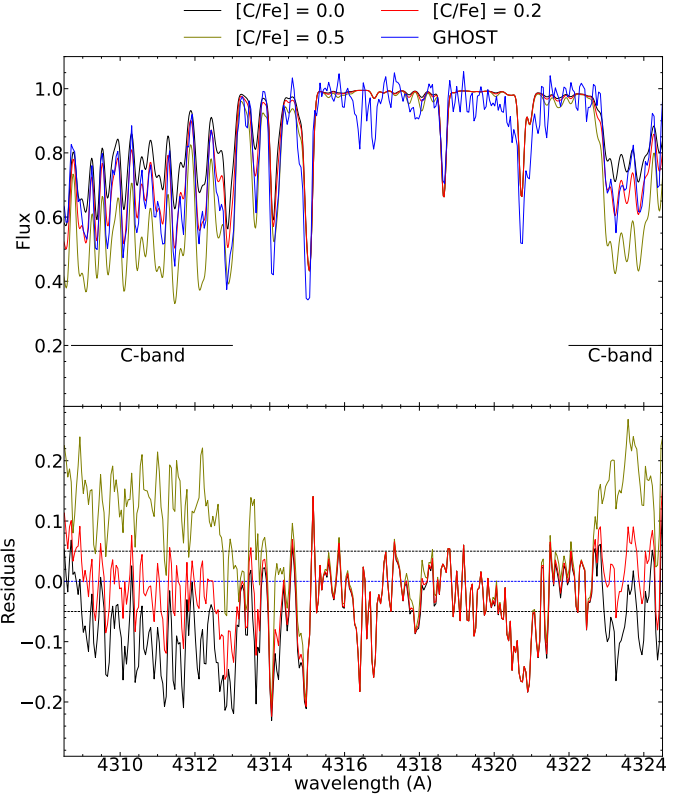


Figure 2. Carbon synthesis. Top panel: The observed spectrum of P180956 is marked with a blue line, while synthetic spectra are denoted by black ($[\text{C}/\text{Fe}] = 0.0$), red ($[\text{C}/\text{Fe}] = 0.2$, best fit), and olive ($[\text{C}/\text{Fe}] = 0.5$) lines. Bottom panel: Residuals of the fits. Horizontal dashed lines mark the null difference (blue) and the dispersion around the continuum (± 0.05 dex, black). The residuals of the best fit (red line) in the regions of Carbon bands are within or similar to the level of the continuum dispersion.

4.2 α -elements

The α -elements producing detectable lines in this star are Mg, Si, Ca, and Ti. The $A(\text{Mg I})$ is from two lines of the Mg I Triplet ($\lambda\lambda 5172.684, 5183.604 \text{ \AA}$) and from other 5 lines for which the SNR is high. Si I is detected from the 4102.936 Å line, which is blended with the wing of the broader H δ line. The $A(\text{Ca I})$ is inferred from 17 spectral lines, from 4200 Å to 6500 Å. The Ca Triplet has been excluded since it shows strong lines ($> 140 \text{ m\AA}$). Ti I and Ti II are present with 17 and 30 lines, respectively.

4.3 Odd-Z elements

Four odd-Z elements are detectable in the GHOST spectrum of this object, Na, Al, K and Sc. Na I is present with the Na I Doublet ($\lambda\lambda 5889.951, 5895.924 \text{ \AA}$). The Na I D lines from the interstellar medium are not affecting the stellar component, in agreement with Sestito et al. (2023b). The combination of the wide spectral coverage of GHOST and its efficiency in the blue region of the spectrum allows us to detect the 2 lines of Al I $\lambda\lambda 3944.006, 3961.520 \text{ \AA}$. K I is observable with two lines at $\lambda\lambda 7664.899, 7698.965 \text{ \AA}$, which are usually close to water vapour lines of the Earth's atmosphere. In this case,

⁷ <https://www.as.utexas.edu/~chris/moog.html>

⁸ <https://marcs.astro.uu.se>

the K I spectral lines are well separated from the telluric lines. Sc is present with 6 Sc II lines from 4200 to 5700 Å.

4.4 Fe-peak elements

The Fe-peak elements that are observable in the GHOST spectra of this target are Fe, V, Cr, Mn, Co, Ni, Cu and Zn. A(Fe I) and A(Fe II) are measured from 188 and 15 lines, respectively. V I is present with the 4379.230 Å line. Cr I and Cr II are detected from 8 and 1 line (4558.650 Å), respectively. A(Mn I) is from 7 lines between 4000 to 4850 Å. A(Co I) is measured from 4 lines in the blue from 3800 to 4150 Å. Ni I is detected from the $\lambda\lambda 5476.904, 6643.630$ Å lines. An upper limit on A(Cu I) is obtained with the synthesis on the $\lambda\lambda 5105.541, 5782.132$ Å lines, $[\text{Cu/Fe}] < -0.2$. Only line 4810.528 Å of Zn I is present in this GHOST spectrum.

4.5 Neutron-capture process elements

The blue coverage of the GHOST instrument is essential to detect the neutron-capture process elements in the spectrum of this very metal-poor star, namely Sr, Y, Ba, La, and Eu. Sr II is observed from the $\lambda\lambda 4077.709, 4215.519$ lines. A(Y II) is measured with the SYNTH mode in MOOG from the $\lambda\lambda 4398.010, 4900.119, 4883.682, 5200.409$ Å, giving an upper limit of $[\text{Y/Fe}] < 0.0$. The synthesis of Ba II is made from 4 lines, $\lambda\lambda 4554.029, 4934.076, 6141.730, 6496.910$ Å, which provide a value in agreement with the GRACES analysis, $[\text{Ba/Fe}] \sim -1.5$. La II produces very weak lines, $\lambda\lambda 4920.980, 5290.820, 5301.970, 5303.530$ Å, resulting in a high upper limit, $[\text{La/Fe}] < 0.5$. The Eu II lines, $\lambda\lambda 4129.700, 4205.050$ Å, are hard to detect, giving an upper limit of $[\text{Eu/Fe}] < 0.0$. Other species of neutron-capture elements have been inspected, e.g., Nd and Tb. They present lines at the level of the noise, resulting in uninformative and very high upper limits.

4.6 Non-Local Thermodynamic Equilibrium corrections

The atmosphere of VMP stars are affected by non-local thermodynamic equilibrium (NLTE) effects, which can be large for some species. NLTE corrections have been applied to Fe I and Fe II (Bergemann et al. 2012a), Mg I (Bergemann et al. 2017), Si I (Bergemann et al. 2013), Ca I (Mashonkina et al. 2017a), Ti I and Ti II (Bergemann 2011), Cr I (Bergemann & Cescutti 2010), Mn I (Bergemann et al. 2019), and Co I (Bergemann et al. 2010) using the MPIA data base⁹. For Na I (Lind et al. 2012) and Sr II (Bergemann et al. 2012b), the INSPECT¹⁰ webtool was used. Note that NLTE corrections for Sr II are not available for a star with the stellar parameters of P180956, therefore, the closest parameters $\log g = 2.3$ (vs. 1.87 ± 0.10) and $v_{\text{micro}} = 1.0 \text{ km s}^{-1}$ (vs. $1.5 \pm 0.1 \text{ km s}^{-1}$) provide a negligible correction of ~ -0.01 dex. Similarly, Ba II NLTE corrections, adopted from Mashonkina & Belyaev (2019), are not available for this star. The closest match in their

Table 2. Chemical abundances $[\text{X/H}]$ in LTE, their uncertainties, $\sigma_{[\text{X/H}]}$, already divided by the square root of the number of lines, the number of spectral lines used N_{lines} , and the NLTE corrections $\Delta_{\text{NLTE}} = [\text{X/H}]_{\text{NLTE}} - [\text{X/H}]_{\text{LTE}}$.

Species	$[\text{X/H}]_{\text{LTE}}$	$\sigma_{[\text{X/H}]}$	N_{lines}	Δ_{NLTE}
Fe I	-1.95	0.02	188	+0.148
Fe II	-1.64	0.04	15	+0.004
C	-1.80	0.10	—	—
Na I	-2.38	0.05	2	-0.457
Mg I	-1.94	0.09	7	+0.089
Al I	-2.20	0.25	2	—
Si I	-1.25	0.10	1	+0.040
K I	-1.40	0.13	2	-0.300
Ca I	-2.03	0.05	17	+0.173
Sc II	-1.23	0.07	6	—
Ti I	-1.81	0.04	17	+0.509
Ti II	-1.27	0.03	30	-0.038
V I	-2.07	0.10	1	—
Cr I	-2.23	0.04	8	+0.382
Cr II	-1.87	0.10	1	—
Mn I	-2.40	0.05	7	+0.381
Co I	-1.59	0.21	4	+0.583
Ni I	-1.82	0.04	2	—
Cu I	< -2.20	—	2	—
Zn I	-1.66	0.10	1	—
Sr II	-2.25	0.01	2	-0.011
Y II	< -2.00	—	4	—
Ba II	-3.50	0.10	4	< 0.05
La II	< -1.50	—	4	—
Eu II	< -2.00	—	2	—

online database¹¹ gives a minor correction of $\lesssim 0.05$. NLTE corrections for K are obtained from Ivanova & Shimanskiĭ (2000), which also include hyperfine structure corrections. We highlight that NLTE corrections on Fe, Ti, and Cr are helpful to obtain the ionisation balance among these species, i.e., $A(\text{X I}) \approx A(\text{X II})$.

Table 2 reports the chemical abundances ratios in LTE, $[\text{X/H}]_{\text{LTE}}$, their uncertainties, the number of lines used, and the average NLTE corrections, Δ_{NLTE} .

4.7 Comparison with the GRACES spectral analysis

One of the reasons that this star P180956 was selected as a GHOST commissioning target was its unusually low $[\text{Na/Mg}]$, $[\text{Ca/Mg}]$, and $[\text{Ba/Fe}]$ ratios, either in LTE or NLTE. Thus, we examine our abundance results from this improved GHOST spectrum in comparison to those from the more limited GRACES spectrum.

In general, the chemical abundance results from the GHOST spectra are similar to those from the previous GRACES analysis, as seen in Figure 3, both in LTE. The agreement is excellent for the majority of the elements

⁹ <https://nlte.mpia.de>

¹⁰ <http://www.inspect-stars.com>

¹¹ <http://www.inasan.ru/~lima/pristine/ba2/>

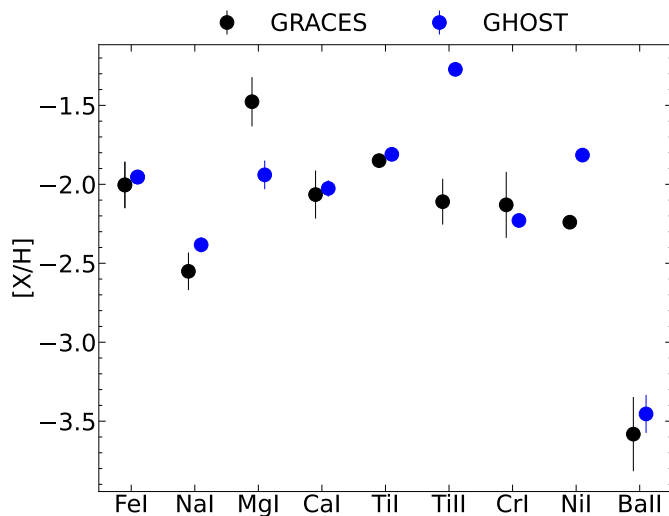


Figure 3. GHOST vs. GRACES chemical abundances, $[X/H]$. GRACES abundances are from [Sestito et al. \(2023b\)](#). Both datasets are in LTE. Points are slightly offset in the horizontal direction to better show their errorbars. Uncertainties on GHOST data are often smaller than the size of the marker.

($\lesssim 2\sigma$), as expected given that we have adopted the same stellar parameters and model atmospheres analysis methods. Furthermore, EW measurements of lines in common to both analyses are similar, to within $\sim 5 - 10$ percent. The better quality of the GHOST spectrum at all wavelengths and the larger number of lines produce a smaller line-to-line dispersion, and, therefore, smaller uncertainties on $[X/H]$.

Our Fe I abundance from GHOST is determined from 188 lines, whereas the GRACES analysis included only 63 lines, in which the mean Fe I abundance changes by only 0.05 dex, and the line-to-line scatter improves by a factor of ~ 1.5 .

Larger differences ($\gtrsim 3\sigma$) are found for Mg I, Ti II, and Ni I, primarily due to the addition of many new spectral lines, which alter the average $A(X)$, and the lower noise around spectral lines.

The revised ratios are $[\text{Na}/\text{Mg}]_{\text{NLTE}} = -0.99 \pm 0.10$ and $[\text{Ca}/\text{Mg}]_{\text{NLTE}} = -0.01 \pm 0.10$. Comparing the other α -elements to Mg, this star shows $[\text{Si}/\text{Mg}]_{\text{NLTE}} = +0.64 \pm 0.10$ and $[\text{Ti}/\text{Mg}]_{\text{NLTE}} = +0.55 \pm 0.10$. Thus, P180956 exhibits very low $[\text{Na}/\text{Fe}]$, slightly sub-solar $[\text{Mg}, \text{Ca}/\text{Fe}]$, enhanced $[\text{Si}, \text{Ti}/\text{Mg}]$, in addition to a very low Ba-content. This is a somewhat unusual chemical abundance pattern for a typical MW halo or bulge star.

4.8 Comparisons with the MW halo and bulge

The chemical abundances of P180956 are compared to a compilation of stars in the MW bulge and halo in Figure 4. The panels in the figure are arranged in order of increasing proton number of the species. The MW bulge compilation (small light blue circles) includes results from [Howes et al. \(2014, 2015, 2016\)](#), [Koch et al. \(2016\)](#), [Reggiani et al. \(2020\)](#), and [Lucey et al. \(2022\)](#). The MW halo compilation (small grey squares) consists of stars obtained from the Stellar

Table 3. Pericentric and apocentric distances (R_{peri} , R_{apo}), the eccentricity (ϵ), the maximum excursion from the plane (Z_{max}), and the vertical component of the angular momentum (L_z) are reported.

Quantity	Bar	No Bar
R_{peri} (kpc)	0.67 ± 0.21	0.73 ± 0.18
R_{apo} (kpc)	12.82 ± 1.06	12.67 ± 0.74
ϵ	0.90 ± 0.03	0.89 ± 0.02
Z_{max} (kpc)	2.01 ± 0.35	2.02 ± 0.33
L_z (kpc km s $^{-1}$)	307.0 ± 83.0	303.0 ± 85.0

Abundances for Galactic Archaeology database¹² (SAGA, [Suda et al. 2008](#)), with high-resolution analysis and no lower or upper limits on the measurements. Both the compilations are from LTE analyses.

The chemical ratios of $[\text{Na}, \text{Mg}, \text{Ca}, \text{Sr}, \text{Ba}/\text{Fe}]$ and upper limit for $[\text{Eu}/\text{Fe}]$ in P180956 are situated at the lower end of the distribution observed in the MW halo and bulge. This is particularly evident for $[\text{Ba}/\text{Fe}]$, which is nearly 2 dex lower than the majority of stars at the same $[\text{Fe}/\text{H}]$. In contrast, $[\text{Si}, \text{Ti}, \text{Sc}, \text{Co}/\text{Fe}]$ ratios in P180956 are slightly enhanced compared to the literature compilations for the MW. Other upper limits (Cu, Y, La) do not provide significant constraints on the abundances.

5 GALACTIC ORBIT

Orbital parameters are derived using GALPY code ([Bovy 2015](#)), integrating the orbit for 1 Gyr in the future and in the past. Uncertainties are determined through a Monte Carlo simulation (1000 iterations) on the input quantities, drawn from a Gaussian distribution. Two Galactic gravitational potentials are adopted and the relative orbits are displayed in Figure 5. One potential corresponds to the model used in [Sestito et al. \(2023b\)](#), which includes a rotating bar (red line); the second is without the bar as in [Sestito et al. \(2019\)](#).

In both cases, P180956 exhibits a slightly prograde orbit (vertical angular momentum $L_z \sim 300$ kpc km s $^{-1}$), which is confined to the Milky Way plane ($Z_{\text{max}} \sim 2$ kpc). The pericentric ($R_{\text{peri}} \sim 0.7$ kpc) and apocentric ($R_{\text{apo}} \sim 13$ kpc) distances indicate that the star's trajectory takes it very close to the Galactic centre before venturing far beyond the Sun's position, resulting in an orbit characterised by high eccentricity ($\epsilon \sim 0.9$). These results are in agreement within 1σ with the previous orbital analysis from [Sestito et al. \(2023b\)](#).

Table 3 reports pericentric and apocentric distances, the eccentricity, the maximum excursion from the plane, the vertical component of the angular momentum as calculated using both gravitational potentials.

6 DISCUSSION

P180956 has peculiar kinematics that indicate that the star is confined to the Milky Way plane on a very eccentric or-

¹² <http://sagadatabase.jp>

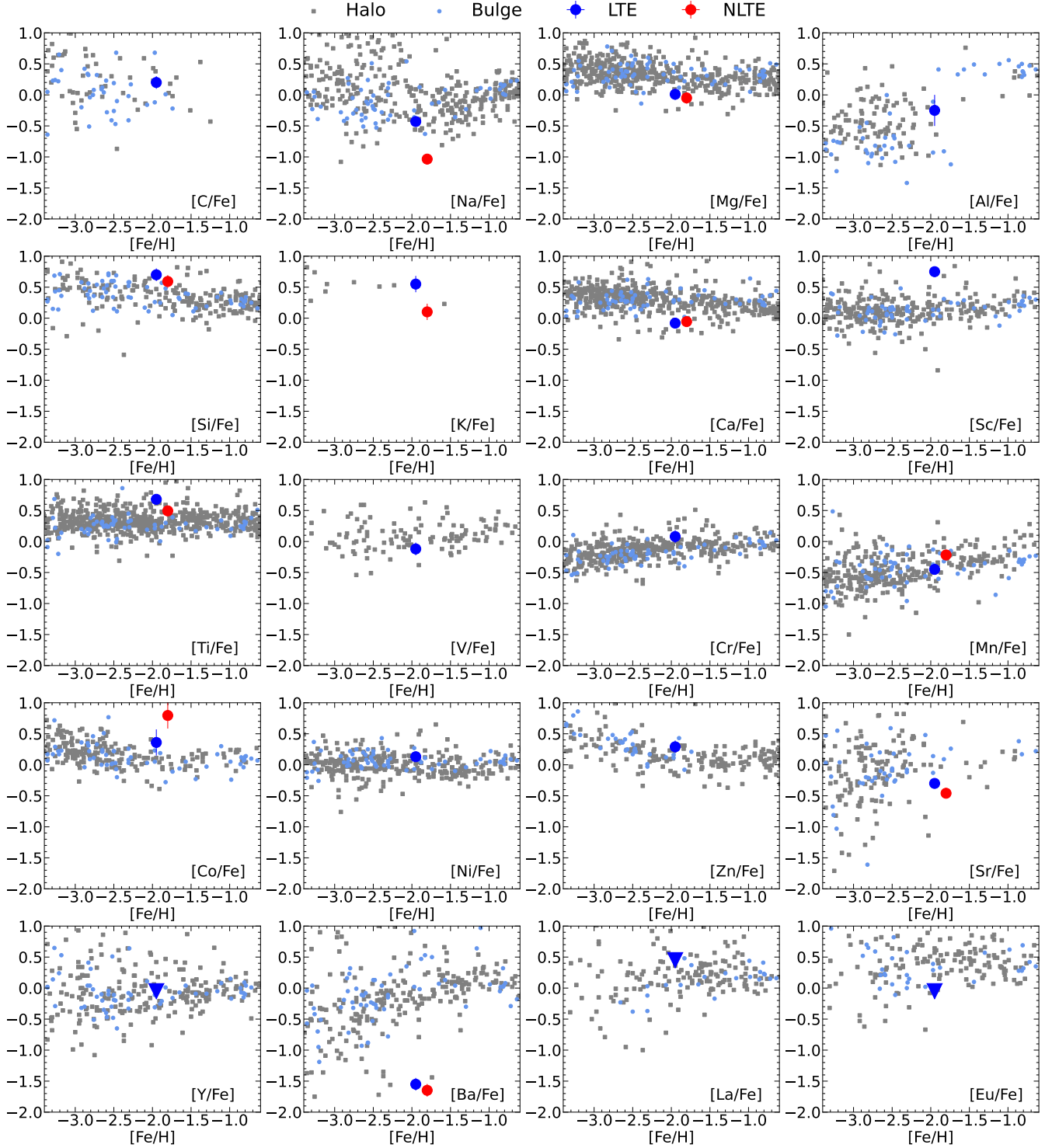


Figure 4. Chemical abundances. Blue and red circles represent the chemical abundances of P180956 in LTE and NLTE-corrected, respectively. Blue triangles denote upper limits for P180956. Small light blue circles represent the bulge compilation (Howes et al. 2014, 2015, 2016; Koch et al. 2016; Reggiani et al. 2020; Lucey et al. 2022), while small grey squares correspond to the halo compilation from the SAGA database (Suda et al. 2008). The uncertainties on $[X/Fe]$ for P180956 are often smaller than the symbol size. The scarcity of literature stars in the $[K/Fe]$ panel may be attributed to the difficulty in measuring K spectral lines in the optical range, as they can be blended with telluric water vapour lines.

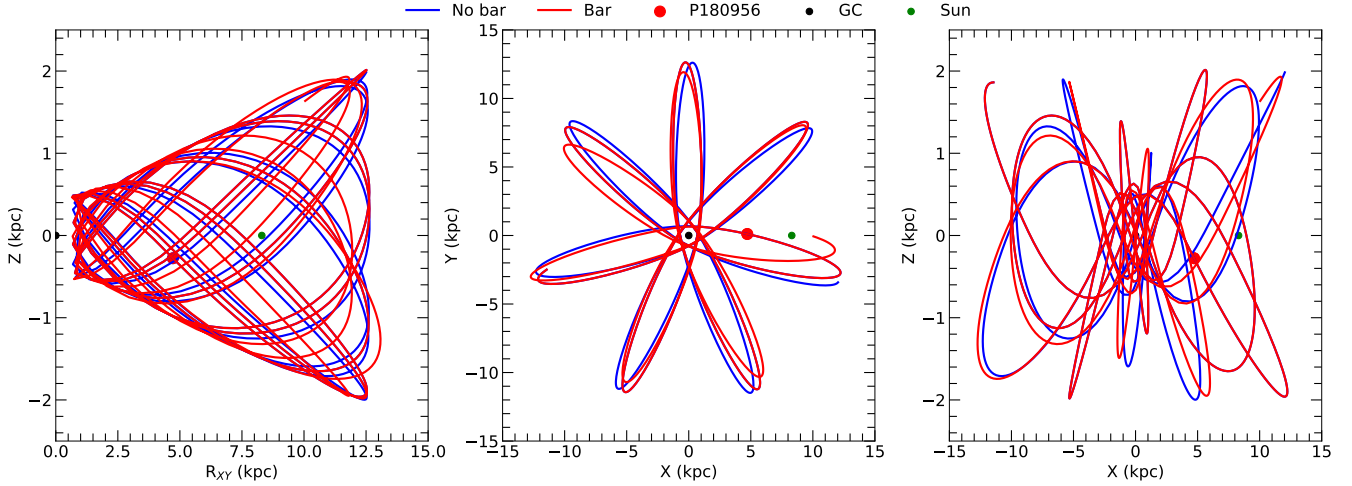


Figure 5. Galactic orbit of P180956. Left panel: Height from the plane Z vs. in-plane projected distance R_{XY} . Central panel: Y vs. X Galactic positions. Right panel: Z vs. X Galactic positions. Red and blue lines represent the orbit integrated in a gravitational potential with and without the presence of a rotating bar as in Sestito et al. (2023b) and as in Sestito et al. (2019), respectively. The red, black and green circles mark the position of P180956, of the Galactic centre (GC), and of the Sun at the present day.

bit, reaching both the very inner region of the MW and a position well beyond the Sun (see Figure 5).

Furthermore, P180956 showed a very low amount of $[\text{Ba}/\text{Fe}]$, $[\text{Ca}/\text{Mg}]$, and $[\text{Na}/\text{Mg}]$. These signatures stand out when compared to MW halo stars, and resemble the abundances of stars found at present in ultra-faint dwarf galaxies. Low chemical abundance ratios in the elements listed above have been interpreted as a sign of contributions from a small number of low-mass supernovae type II (SNe II) in the past, e.g., the so-called "one-shot" model (Frebel et al. 2010a). Therefore, the interpretation of the chemo-dynamical properties from the GRACES spectrum implied that this star may have formed in an ancient dwarf galaxy accreted very early in the MW formation. In the following subsections, a revised and more thorough discussion on the origin of this star and on the properties of its formation site is presented.

6.1 The yields of the supernovae progenitors

The wavelength coverage of GHOST and the SNR of the observed spectra allow the detection of up to 18 chemical species and four meaningful upper limits, for a total of 13 elements beyond those available in the previous GRACES spectral analysis. Comparing this extensive set of chemical abundances with the predicted yields of supernovae from theoretical models can be used for insights into the nucleosynthetic processes that occurred at the formation site of P180956. To accomplish this, the online tool STARFIT¹³ is used. The yields of best fit are obtained by combining the supernovae II yields of the best solutions chosen from a pool of theoretical models. A total of ten models have been selected, encompassing various types of supernovae events, i.e., hypernovae, core-collapse, rotating massive stars, neutron stars mergers, and pair-instability SNe.

The theoretical yields $[X/H]$ from contributing SNe are

compared with the observational data in the top panel of Figure 6. The scaled solar abundances ratios (black line) are from Asplund et al. (2009), shifted to match the $[\text{Fe}/H]$ of P180956. These fail to reproduce our data, except for Fe (by design), Na, and Mg. The solar abundances pattern predicts a net decrease in the yields from Si, which is not seen in P180956.

The best fit solution (magenta line) from STARFIT consists in five SNe II events originating from Population III stars. This fit is a mixture of three low-mass hypernovae¹⁴ with $M \sim 10 M_{\odot}$ (Heger & Woosley 2010; Heger et al. 2012), one around $M \sim 15 M_{\odot}$ (Limongi & Chieffi 2018), and one intermediate-mass ($\sim 80 M_{\odot}$) fast-rotating ($\sim 300 \text{ km s}^{-1}$) supernova (Grimmett et al. 2018). The second best fit (orange line) solution is composed of three events, two low-mass hypernovae with $M \sim 10 - 17 M_{\odot}$ (Heger & Woosley 2010; Heger et al. 2012) and one fast-rotating ($\sim 300 \text{ km s}^{-1}$) SN with $M \sim 120 M_{\odot}$ (Limongi & Chieffi 2018).

The difference between the observed $[X/H]$ and the theoretical yields from the best (magenta circles) and second best (orange squares) fits are displayed in the bottom panel of Figure 6. Both solutions provide a difference below $\lesssim 0.3$ in absolute value for the majority of the species.

We want to emphasise that the use of STARFIT is more as an illustration of the range of events that might be needed to explain the chemistry of this star. STARFIT suggests an interpretation that contributions from high-mass supernovae ($> 140 M_{\odot}$, e.g., pair-instability) and neutron-star mergers are ruled out for this star. The former would produce a strong odd-even effect in the yields (Takahashi et al. 2018; Salvadori et al. 2019), i.e., very low $[\text{Na}, \text{Al}/\text{Mg}]$ (~ -1.3) and high $[\text{Ca}/\text{Mg}]$ ($\gtrsim +0.6$); the latter would produce an enrichment in neutron-capture elements (e.g., Cowan et al. 2021). Both scenarios are in contrast with the

¹³ <https://starfit.org>

¹⁴ A hypernova explosion has a typical energy of at least a factor ~ 10 greater than a classical supernova type II.

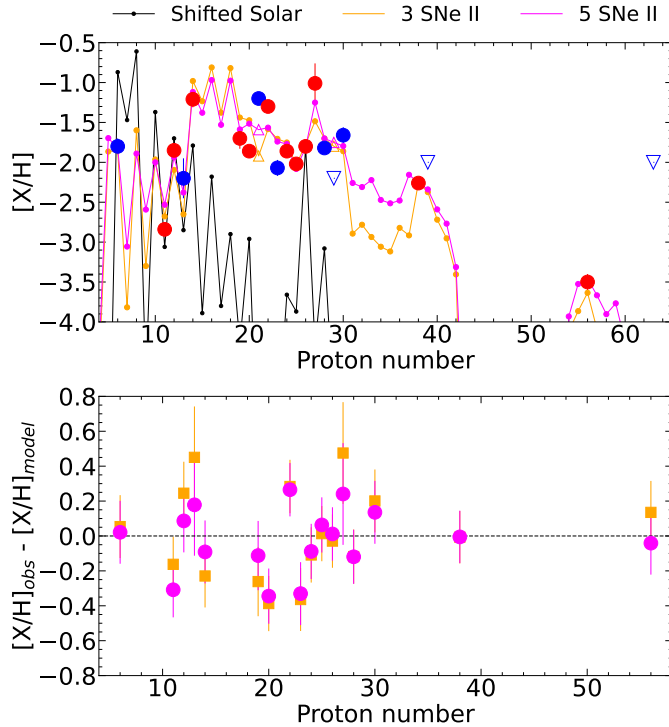


Figure 6. Supernovae yields. Red and blue circles are NLTE and LTE $[X/H]$ of P180956, respectively. Upper limits of Cu, Y, and Eu are marked with empty downward blue triangles. Top panel: Black dots and line represent the solar scaled abundances from [Asplund et al. \(2009\)](#) shifted to match the $[Fe/H]$ of P180956. Magenta and orange dots and lines represent the theoretical yields from the best (5 SNe II events) and second best fit (3 SNe II events), respectively. Lower limits of Sc and Cu in the theoretical models are denoted with empty upward triangles. Bottom panel: The difference between the observed $[X/H]$ and the yields predicted by the best (magenta circles) and second best (orange squares) fit from STARFIT. Upper limits in the data and lower limits in the modelled yields are removed. Uncertainties on the data are summed in quadrature to 0.15 for the theoretical yields. The horizontal dashed line marks the null difference.

observed chemical properties of P180956. STARFIT suggests that the main contributing SNe II are in the low-mass range. Specifically, hypernovae are necessary to produce the high $[Si, Ti/Mg]$ ratios. These findings align with the scenario proposed by [Ishigaki et al. \(2018\)](#), where low-mass hypernovae ($\lesssim 40 M_{\odot}$) are the primary sources of enrichment of the interstellar medium during the early stages of chemical evolution. In addition, the presence of one fast-rotating intermediate-mass supernova is needed to well reproduce the pattern of the heavy elements, i.e., Sr, Ba.

6.2 In-situ vs. accreted diagnostics

What if this star formed in-situ, i.e., in the proto-disc but after the early Galactic assembly? The period between the early MW assembly and the formation of the disc, dubbed "Aurora" ([Belokurov & Kravtsov 2022](#)), has been proposed to be very chaotic, forming bound massive clusters, chemically similar to globular clusters ([Belokurov & Kravtsov 2023](#)). This implies that some Aurora stars would be en-

riched in N, Na, and Al, while others would resemble the "normal" halo stars ([Belokurov & Kravtsov 2023](#)). P180956 is Na-poor, Al-normal, and r-process poor, with the latter being very rare for halo stars at that metallicity (see Figure 4). This chemical pattern rules out the "Aurora" as the origin for P180956.

Other studies have suggested $[Mg/Mn]$ vs. $[Al/Fe]$ as a diagnostic to differentiate accreted stars from in-situ stars (e.g., [Das et al. 2020](#); [Horta et al. 2021](#)). Figure 7 illustrates this chemical space, including APOGEE DR17 ([Abdurro'uf et al. 2022](#)) stars for comparison. Dashed black lines delineate three regions where accreted, in-situ low- α , and in-situ high- α stars are more likely to be found (e.g., [Das et al. 2020](#); [Horta et al. 2021](#)). In the LTE case, P180956 lies close to the centre of the accreted "blob", while considering NLTE corrections, the star falls into the in-situ low- α region.

Recently, [Horta et al. \(2023\)](#) provide a summary of the chemo-dynamical properties of known accreted structures based on the latest Gaia and APOGEE data releases. Their Figure 13 displays the $[Mg/Mn]$ vs. $[Al/Fe]$ space for all the accreted known structures, showing that some of their stars have $[Mg/Mn] \sim 0.0$ or even negative (e.g., Sagittarius, Sequoia, Gaia-Sausage-Enceladus). Therefore, part of the in-situ low- α region, is actually accreted. The accreted region in Figure 7 is here tentatively extended (accreted low- α), by lengthening the dashed green line, which suggests that P180956 is of accreted origin. Offsets between the NLTE infra-red (APOGEE) and the NLTE-corrected optical analyses are estimated to be $\Delta[Mg/Mn] = +0.15 \pm 0.18$ and $\Delta[Al/Fe] = -0.11 \pm 0.12$ ([Jönsson et al. 2020](#)). These corrections, not applied in Figure 7, would move P180956 more closely to the accreted low- α "blob".

Can P180956 be associated with any of the recently discovered accreted structures? The system that bears the closest resemblance to P180956 in terms of kinematical properties (see [Horta et al. 2023](#)) is Gaia-Sausage-Enceladus (GSE, e.g., [Helmi et al. 2018](#); [Belokurov et al. 2018](#)). The high eccentric orbit of GSE (0.93 ± 0.06) and its mean pericentric and apocentric distances ($r_{\text{peri}} = 0.61 \pm 1.03$ kpc and $r_{\text{apo}} = 17.15 \pm 5.22$ kpc) are compatible with P180956's orbital parameters within 1σ (see Table 3). However, stars of GSE reach a maximum height from the plane that is typically greater than the one of our target ($Z_{\text{max}} = 9.84 \pm 6.14$ kpc vs. $Z_{\text{max}} = 2.01 \pm 0.35$ kpc).

[Helmi et al. \(2018\)](#) demonstrate that the GSE population has lower $[\alpha/Fe]$ ratios compared to stars in the MW halo. Similarly, [Hayes et al. \(2018\)](#) provide evidence for a low- α population, showing that its stars exhibit $[Mg, Si/Fe]_{\text{NLTE}} \sim 0.25 - 0.30$ at the $[Fe/H]$ of P180956. However, these ratios are not compatible with the values of our target, which have $[Mg/Fe]_{\text{NLTE}} = -0.05 \pm 0.09$ and $[Si/Fe]_{\text{NLTE}} = +0.59 \pm 0.10$. Thus, the chemo-dynamical properties of P180956 differ from those of GSE and other known accreted structures.

6.3 Origin in an ultra-faint dwarf galaxy

A comparison of the neutron-capture elements $[Sr/Fe]$ and $[Ba/Fe]$ vs. $[Fe/H]$ for P180956, stars from ultra-faint dwarf (UFDs), from classical dwarf galaxies (DGs), and Milky Way halo is presented in the left panels of Figure 8. It is evident that P180956 exhibits lower $[Sr, Ba/Fe]$ (and $[Eu/Fe]$ from

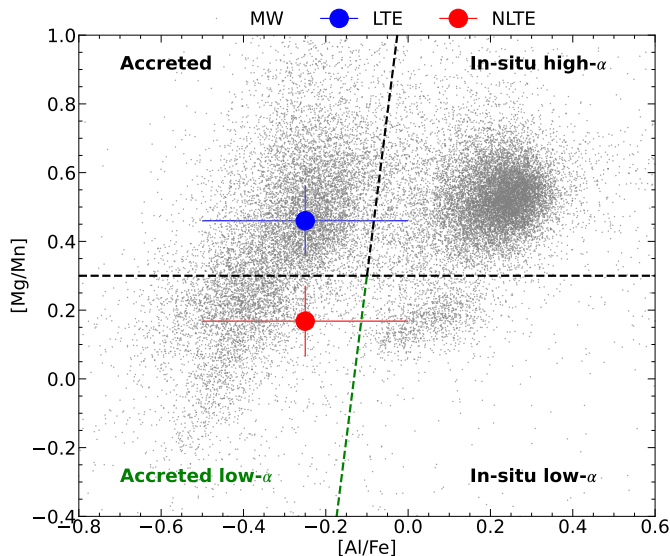


Figure 7. $[\text{Mg}/\text{Mn}]$ vs. $[\text{Al}/\text{Fe}]$ space. P180956 data are shown in blue and red in LTE and NLTE-corrected ($[\text{Mg}/\text{Mn}]$ only), respectively. Small grey dots are APOGEE DR17 MW stars selected to have $\text{SNR} > 70$ and $[\text{Fe}/\text{H}] < -0.7$, which are derived from an NLTE analysis. The three regions delimited by the dashed black lines, accreted and in-situ low-/high- α are defined following Das et al. (2020) and Horta et al. (2021). The accreted region has been prolonged following the dashed green line, in which accreted low- α stars should lie.

Figure 4) ratios than the majority of MW halo stars at the same metallicity. The $[\text{Sr}/\text{Fe}]$ of P180956 is similar to the bulk value of DGs, while UFDs have lower values. On the opposite behaviour is $[\text{Ba}/\text{Fe}]$, where P180956's ratio is similar to those in the low-end distribution of UFDs. The low-abundance of neutron-capture processes elements has been interpreted as the contribution of low-mass supernovae and the absence of neutron stars mergers events (e.g., Cowan et al. 2021). Furthermore, the combinations of stochasticity in the production of neutron-capture elements with the inability of UFDs to retain metals can explain the low $[\text{Sr}, \text{Ba}, \text{Eu}/\text{Fe}]$ observed in these systems (e.g., Venn et al. 2012; Ji et al. 2019).

The distribution of $[\text{Sr}/\text{Ba}]$ vs. $[\text{Ba}/\text{Fe}]$ is shown in the right panel of Figure 8. Halo stars exhibit a downward trend as $[\text{Ba}/\text{Fe}]$ increases (Mashonkina et al. 2017b), albeit mostly clumped around $[\text{Sr}/\text{Ba}] \sim 0.3$ (Ji et al. 2019). Both UFDs and DGs present a wide distribution in $[\text{Sr}/\text{Ba}]$ (up to ~ 1.5 dex), with UFDs populate a distinct region from the majority of MW halo stars and of DGs (Mashonkina et al. 2017b; Roederer 2017; Ji et al. 2019; Reichert et al. 2020; Sitnova et al. 2021). P180956 has a relatively high $[\text{Sr}/\text{Ba}]$ ratio, close to the upper-end of the distributions of the MW halo, Coma Berenices (UFD), and Sculptor (DG), while its $[\text{Ba}/\text{Fe}]$ is typical of an UFD's star.

Did this star originate in an UFD or in classical DG? At the metallicity of P180956, DGs would likely involve contributions from asymptotic giant branch stars (AGBs) and, in some cases, SNe Ia. AGBs would produce Ba via s-process nucleosynthesis (e.g., Pignatari et al. 2008; Cescutti & Chiappini 2014), reaching solar values. Additional

contribution from SNe Ia would lower the overall $[\alpha/\text{Fe}]$ ratios to solar or sub-solar values. Given P180956 has a very low-Ba ($[\text{Ba}/\text{Fe}]_{\text{NLTE}} \sim -1.7$) and the inhomogeneity in the α -elements ($[\text{Si}, \text{Ti}/\text{Mg}, \text{Ca}] \sim 0.5$), the contributions of AGBs and SNe Ia are likely ruled out, and, as well, the DG scenario.

How to explain the high $[\text{Sr}/\text{Ba}]$? Mashonkina et al. (2017b) discuss that sub-solar $[\text{Sr}/\text{Ba}]$ implies that both elements are produced solely by r-process, while solar- and supersolar- $[\text{Sr}/\text{Ba}]$ indicate the involvement of s-processes in the Sr production. Various kinds of supernovae events have been proposed to explain the relative excess of Sr compared to other neutron-capture elements (Mashonkina et al. 2017b, and references therein). Hypernovae (Izutani et al. 2009) and s-process nucleosynthesis in low-metallicity fast-rotating supernovae (Pignatari et al. 2008; Banerjee et al. 2018; Grimmett et al. 2018; Limongi & Chieffi 2018) are also listed among these, which are always invoked by the best fit models from STARFIT (see Section 6.1). Thus, the interpretation that P180956 originated in a UFD is further supported by the new chemical abundance analysis and preferred over the DG hypothesis.

6.4 P180956, witness of the early Galactic assembly

Above we have outlined the most likely origin for P180956 as from an accreted UFD. Two new questions now arise whether the star was brought in during the early Galactic assembly or later on and if its system was isolated or brought in with one of the massive known accreted satellites.

P180956 was also selected for GHOST commissioning because of its peculiar orbital parameters, as it remains relatively close to the MW plane (see Figure 5). Recently, the presence of this population has been observed from the ultra metal-poor regime (UMP, $[\text{Fe}/\text{H}] \leq -4.0$, Sestito et al. 2019) to the disc's metallicity (Sestito et al. 2020; Di Matteo et al. 2020; Venn et al. 2020; Cordoni et al. 2021; Mardini et al. 2022), finding that the majority of them moves in a prograde orbit. While VMP "planar" stars have been dynamically detected in various investigations, thorough and detailed analyses of their chemical properties are scarce.

The existence of this population has also been explored through high-resolution cosmological zoom-in simulations (Sestito et al. 2021; Santistevan et al. 2021). The simulations¹⁵ predict the presence of a "planar" population. While previous observational studies focused on the origin of low-eccentricity stars, Sestito et al. (2021) also discussed that the more eccentric members of the planar population are likely brought in during the early-assembly phase. This is because, during that epoch, the gravitational potential of the forming proto-Galaxy is still shallow, allowing for the deposit of accreted systems into the inner regions. The relatively small excursion from the MW plane, the pericentric and apocentric distances, in addition to the high eccentricity suggest that the star was brought in during the early-assembly phase.

¹⁵ Sestito et al. (2021) utilised the NIHAO-UHD simulations (Buck et al. 2019), while Santistevan et al. (2021) employed the FIRE simulations (Hopkins et al. 2018).

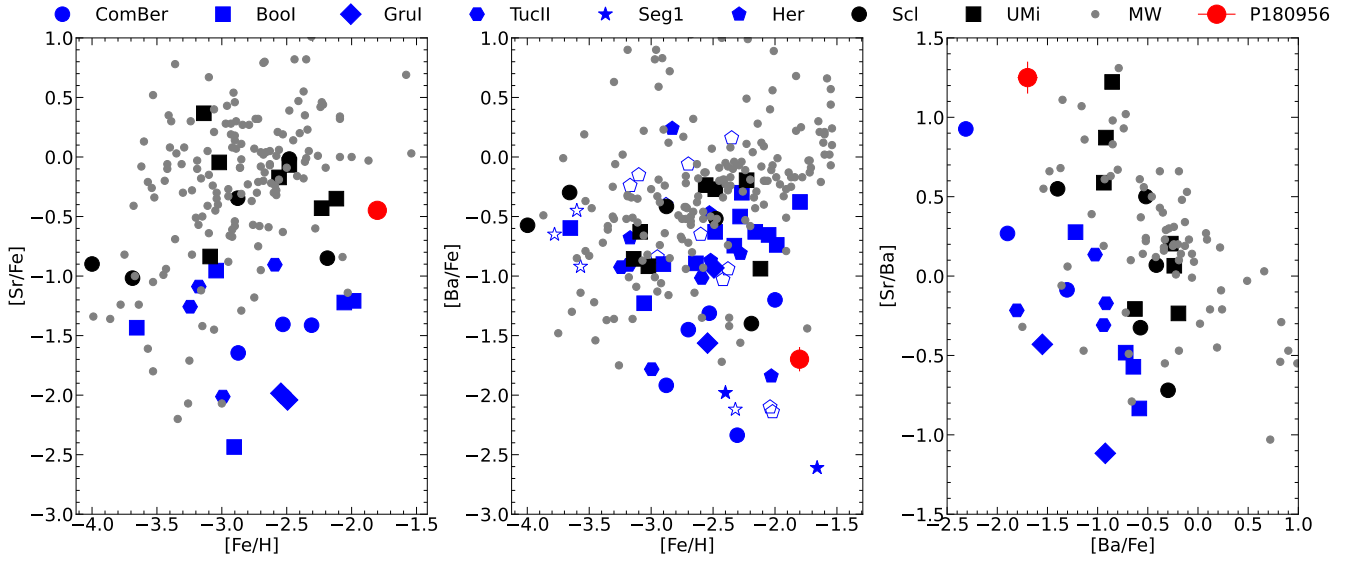


Figure 8. Neutron-capture elements. Left panel: $[\text{Sr}/\text{Fe}]$ vs. $[\text{Fe}/\text{H}]$. Central panel: $[\text{Ba}/\text{Fe}]$ vs. $[\text{Fe}/\text{H}]$. Empty symbols denote upper limits on the vertical axis. Right panel: $[\text{Sr}/\text{Ba}]$ vs. $[\text{Ba}/\text{Fe}]$. The red circle marks the NLTE-corrected chemical ratios of P180956. MW stars are from the SAGA database (Suda et al. 2008); Coma Berenice (ComBer) stars are from Frebel et al. (2010b) and Waller et al. (2023); Bootes I (BooI) stars are from Feltzing et al. (2009), Norris et al. (2010), Gilmore et al. (2013), Ishigaki et al. (2014), and Frebel et al. (2016); Gru I stars are from Ji et al. (2019); Tucana II (TucII) stars are from Ji et al. (2016) and Chiti et al. (2018); Segue 1 (Seg1) stars are from Frebel et al. (2014); Hercules (Her) stars are from Koch et al. (2008), Koch et al. (2013), and François et al. (2016); Sculptor (Scl) and Ursa Minor (UMi) stars are from Mashonkina et al. (2017b).

In Section 6.2, we rule out that P180956 formed in one of the known accreted structures, however, given 1) that some of its orbital parameters are similar to those of GSE (except for Z_{max}), 2) its formation likely in an UFD-like system (see Section 6.3), and 3) its early accretion to the MW, two scenarios on the origin of P180956 are proposed. The first is that P180956 originate in one of the many low-mass building blocks that formed the proto-MW, which had chemical and physical properties similar to those of present UFDs; the second is that its progenitor system was an UFD satellite of GSE, that has been brought in into the inner Galaxy during the infall of GSE.

7 CONCLUSIONS

This work represents the second high-resolution spectroscopic analysis utilising the GHOST spectrograph mounted at Gemini South, following the detailed analysis of two r-process rich stars in the Reticulum II ultra-faint dwarf galaxy (Hayes et al. 2023). The spectra of P180956, a star with unique chemo-dynamical properties, were observed during the second commissioning run of the instrument in September 2022. Previously, the star was observed with GRACES at Gemini North and analysed as part of the Pristine Inner Galaxy Survey (Arentsen et al. 2020a; Sestito et al. 2023b). In this study, we conducted a comprehensive analysis of the chemo-dynamical properties of P180956, leading to the following results:

(i) The high efficiency and wide spectral coverage of the GHOST instrument (see Figure 1) enabled the detection of approximately 20 atomic species (see Figure 4), providing

crucial insights into the origin and chemical properties of P180956 and its formation site.

(ii) The larger number of species and spectral lines available with GHOST facilitated a more accurate and thorough analysis compared to GRACES (see Figure 3) that usually allows the detection of only ~ 10 atomic species (Kielty et al. 2021; Jeong et al. 2023; Sestito et al. 2023b,a; Waller et al. 2023).

(iii) Theoretical models of supernovae yields suggest that the formation site of P180956 experienced pollution from 2 to 4 low-mass hypernovae ($\lesssim 15 M_{\odot}$) and one intermediate-mass ($80 - 120 M_{\odot}$) fast-rotating ($\sim 300 \text{ km s}^{-1}$) supernova (see Figure 6).

(iv) These combinations of supernovae events resulted in a composition of α -elements with solar Ca and Mg abundances and enhanced Si and Ti abundances (see Figures 4 and 6).

(v) The specific combination of supernovae yields led to low abundances of neutron-capture elements (Sr, Ba, Eu), with a relatively high $[\text{Sr}/\text{Ba}]$ ratio (see Figure 8). This can be explained with the additional s-process channels for Sr production that occur in hypernovae and fast-rotating supernovae.

(vi) The low amount amount of neutron-capture elements (see Figures 4 and 8) is rare in the MW halo and typical of stars in ultra-faint dwarf galaxy systems.

(vii) The kinematical properties of P180956 (see Figure 5) suggests the star was likely accreted during the early-assembly phase of the Milky Way. Its $[\text{Mg}/\text{Mn}]$ ratio is also indicative of its accreted origin (see Figure 7).

(viii) None of the known accreted structures exhibit chemo-dynamical properties resembling perfectly those of

P180956. Only Gaia-Sausage-Enceladus has similar eccentricity, apocentric and pericentric distances to P180956.

(ix) P180956 originated in an ancient system chemically similar to present ultra-faint dwarf galaxies, either accreted alone or dragged in with Gaia-Sausage-Enceladus as its satellite.

The advent of the GHOST high-resolution spectrograph has been invoked by various chemo-dynamical investigations targeting the MW and its satellite systems (e.g., Sestito et al. 2023b,a; Waller et al. 2023). This study, along with Hayes et al. (2023), demonstrates that the combination of the Gemini South's large aperture and GHOST's high efficiency and wide spectral coverage is ideal for investigating low-metallicity stars in the Milky Way and nearby systems. The synergy between GHOST and the Gaia satellite will undoubtedly propel Galactic Archaeological studies forward.

ACKNOWLEDGEMENTS

We acknowledge and respect the ʔəwəŋən peoples on whose traditional territory the University of Victoria stands and the Songhees, Esquimalt and WSÁNEĆ peoples whose historical relationships with the land continue to this day.

FS thanks the Dr. Margaret "Marmie" Perkins Hess postdoctoral fellowship for funding his work at the University of Victoria. KAV thanks the National Sciences and Engineering Research Council of Canada for funding through the Discovery Grants and CREATE programs. AA acknowledges support from the Herchel Smith Fellowship at the University of Cambridge and a Fitzwilliam College research fellowship supported by the Isaac Newton Trust. NFM gratefully acknowledge support from the French National Research Agency (ANR) funded project "Pristine" (ANR-18-CE31-0017) along with funding from the European Research Council (ERC) under the European Unions Horizon 2020 research and innovation programme (grant agreement No. 834148). TM acknowledges the Spinoza Grant from the Dutch Research Council (NWO) for supporting his research. ES acknowledges funding through VIDI grant "Pushing Galactic Archaeology to its limits" (with project number VI.Vidi.193.093) which is funded by the Dutch Research Council (NWO). This research was supported by the International Space Science Institute (ISSI) in Bern, through ISSI International Team project 540 (The early Milky Way).

This work is based on observations obtained with Gemini South/GHOST, during the commissioning run of September 2022. Based on observations obtained at the international Gemini Observatory, a program of NSF's NOIR-Lab, which is managed by the Association of Universities for Research in Astronomy (AURA) under a cooperative agreement with the National Science Foundation. On behalf of the Gemini Observatory partnership: the National Science Foundation (United States), National Research Council (Canada), Agencia Nacional de Investigación y Desarrollo (Chile), Ministerio de Ciencia, Tecnología e Innovación (Argentina), Ministério da Ciência, Tecnologia, Inovações e Comunicações (Brazil), and Korea Astronomy and Space Science Institute (Republic of Korea).

This work has made use of data from the European Space Agency (ESA) mission *Gaia* (<https://www.cosmos.esa.int/gaia>), processed by the *Gaia* Data Processing and

Analysis Consortium (DPAC, <https://www.cosmos.esa.int/web/gaia/dpac/consortium>). Funding for the DPAC has been provided by national institutions, in particular the institutions participating in the *Gaia* Multilateral Agreement.

This research has made use of the SIMBAD database, operated at CDS, Strasbourg, France (Wenger et al. 2000). This work made extensive use of TOPCAT (Taylor 2005).

DATA AVAILABILITY

The data underlying this article are available in the article and in its online supplementary material.

REFERENCES

- Abadi M. G., Navarro J. F., Steinmetz M., Eke V. R., 2003, *ApJ*, **597**, 21
- Abdurro'uf et al., 2022, *ApJS*, **259**, 35
- Aguado D. S., et al., 2019, *MNRAS*, **490**, 2241
- Arentsen A., et al., 2020a, *MNRAS*, **491**, L11
- Arentsen A., et al., 2020b, *MNRAS*, **496**, 4964
- Asplund M., Grevesse N., Sauval A. J., Scott P., 2009, *ARA&A*, **47**, 481
- Banerjee P., Qian Y.-Z., Heger A., 2018, *ApJ*, **865**, 120
- Beasley M. A., Leaman R., Gallart C., Larsen S. S., Battaglia G., Monelli M., Pedreros M. H., 2019, *MNRAS*, **487**, 1986
- Belokurov V., Kravtsov A., 2022, *MNRAS*, **514**, 689
- Belokurov V., Kravtsov A., 2023, *arXiv e-prints*, p. [arXiv:2306.00060](https://arxiv.org/abs/2306.00060)
- Belokurov V., Erkal D., Evans N. W., Koposov S. E., Deason A. J., 2018, *MNRAS*, **478**, 611
- Bensby T., et al., 2013, *A&A*, **549**, A147
- Bensby T., et al., 2017, *A&A*, **605**, A89
- Bergemann M., 2011, *MNRAS*, **413**, 2184
- Bergemann M., Cescutti G., 2010, *A&A*, **522**, A9
- Bergemann M., Pickering J. C., Gehren T., 2010, *MNRAS*, **401**, 1334
- Bergemann M., Lind K., Collet R., Magic Z., Asplund M., 2012a, *MNRAS*, **427**, 27
- Bergemann M., Hansen C. J., Bautista M., Ruchti G., 2012b, *A&A*, **546**, A90
- Bergemann M., Kudritzki R.-P., Würl M., Plez B., Davies B., Gazak Z., 2013, *ApJ*, **764**, 115
- Bergemann M., Collet R., Amarsi A. M., Kovalev M., Ruchti G., Magic Z., 2017, *ApJ*, **847**, 15
- Bergemann M., et al., 2019, *A&A*, **631**, A80
- Bessell M., Bloxham G., Schmidt B., Keller S., Tisserand P., Francis P., 2011, *PASP*, **123**, 789
- Bovy J., 2015, *ApJS*, **216**, 29
- Buck T., Obreja A., Macciò A. V., Minchev I., Dutton A. A., Ostriker J. P., 2019, *arXiv e-prints*, p. [arXiv:1909.05864](https://arxiv.org/abs/1909.05864)
- Bullock J. S., Johnston K. V., 2005, *ApJ*, **635**, 931
- Cescutti G., Chiappini C., 2014, *A&A*, **565**, A51
- Chene A.-N., et al., 2014, in Navarro R., Cunningham C. R., Barto A. A., eds, *Society of Photo-Optical Instrumentation Engineers (SPIE) Conference Series* Vol. 9151, *Advances in Optical and Mechanical Technologies for Telescopes and Instrumentation*. p. 915147 ([arXiv:1409.7448](https://arxiv.org/abs/1409.7448)), [doi:10.1117/12.2057417](https://doi.org/10.1117/12.2057417)
- Chiti A., Frebel A., Ji A. P., Jerjen H., Kim D., Norris J. E., 2018, *ApJ*, **857**, 74
- Cordoni G., et al., 2021, *MNRAS*, **503**, 2539

- Cowan J. J., Sneden C., Lawler J. E., Aprahamian A., Wiescher M., Langanke K., Martínez-Pinedo G., Thielemann F.-K., 2021, *Reviews of Modern Physics*, **93**, 015002
- Das P., Hawkins K., Jofré P., 2020, *MNRAS*, **493**, 5195
- Di Matteo P., Spite M., Haywood M., Bonifacio P., Gómez A., Spite F., Caffau E., 2020, *A&A*, **636**, A115
- El-Badry K., et al., 2018, *MNRAS*, **480**, 652
- Evans D. W., et al., 2018, *A&A*, **616**, A4
- Feltzing S., Eriksson K., Kleya J., Wilkinson M. I., 2009, *A&A*, **508**, L1
- François P., Monaco L., Bonifacio P., Moni Bidin C., Geisler D., Sbordone L., 2016, *A&A*, **588**, A7
- Frebel A., Kirby E. N., Simon J. D., 2010a, *Nature*, **464**, 72
- Frebel A., Simon J. D., Geha M., Willman B., 2010b, *ApJ*, **708**, 560
- Frebel A., Simon J. D., Kirby E. N., 2014, *ApJ*, **786**, 74
- Frebel A., Norris J. E., Gilmore G., Wyse R. F. G., 2016, *ApJ*, **826**, 110
- Freeman K., Bland-Hawthorn J., 2002, *ARA&A*, **40**, 487
- Gilmore G., Norris J. E., Monaco L., Yong D., Wyse R. F. G., Geisler D., 2013, *ApJ*, **763**, 61
- González Hernández J. I., Bonifacio P., 2009, *A&A*, **497**, 497
- Green G. M., Schlafly E., Zucker C., Speagle J. S., Finkbeiner D., 2019, *ApJ*, **887**, 93
- Grimmett J. J., Heger A., Karakas A. I., Müller B., 2018, *MNRAS*, **479**, 495
- Gustafsson B., Edvardsson B., Eriksson K., Jørgensen U. G., Nordlund Å., Plez B., 2008, *A&A*, **486**, 951
- Hayes C. R., et al., 2018, *ApJ*, **852**, 49
- Hayes C. R., et al., 2022, in Evans C. J., Bryant J. J., Motohara K., eds, *Society of Photo-Optical Instrumentation Engineers (SPIE) Conference Series Vol. 12184, Ground-based and Airborne Instrumentation for Astronomy IX*. p. 121846H, doi:10.1117/12.2642905
- Hayes C. R., et al., 2023, *arXiv e-prints*, p. arXiv:2306.04804
- Heger A., Woosley S. E., 2010, *ApJ*, **724**, 341
- Heger A., Woosley S., Vo P., Chen K., Joggerst C., 2012, in Aoki W., Ishigaki M., Suda T., Tsujimoto T., Arimoto N., eds, *Astronomical Society of the Pacific Conference Series Vol. 458, Galactic Archaeology: Near-Field Cosmology and the Formation of the Milky Way*. p. 11
- Helmi A., Babusiaux C., Koppelman H. H., Massari D., Veljanoski J., Brown A. G. A., 2018, *Nature*, **563**, 85
- Hopkins P. F., et al., 2018, *MNRAS*, **480**, 800
- Horta D., et al., 2021, *MNRAS*, **500**, 1385
- Horta D., et al., 2023, *MNRAS*, **520**, 5671
- Howes L. M., et al., 2014, *MNRAS*, **445**, 4241
- Howes L. M., et al., 2015, *Nature*, **527**, 484
- Howes L. M., et al., 2016, *MNRAS*, **460**, 884
- Ireland M. J., White M., Bento J. P., Farrell T., Labrie K., Luvaul L., Nielsen J. G., Simpson C., 2018, in Guzman J. C., Ibsen J., eds, *Society of Photo-Optical Instrumentation Engineers (SPIE) Conference Series Vol. 10707, Software and Cyberinfrastructure for Astronomy V*. p. 1070735, doi:10.1117/12.2314418
- Ishigaki M. N., Aoki W., Arimoto N., Okamoto S., 2014, *A&A*, **562**, A146
- Ishigaki M. N., Tominaga N., Kobayashi C., Nomoto K., 2018, *ApJ*, **857**, 46
- Ivanova D. V., Shimanskiĭ V. V., 2000, *Astronomy Reports*, **44**, 376
- Izutani N., Umeda H., Tominaga N., 2009, *ApJ*, **692**, 1517
- Jeong M., Lee Y. S., Beers T. C., Placco V. M., Kim Y. K., Koo J.-R., Lee H.-G., Yang S.-C., 2023, *ApJ*, **948**, 38
- Ji A. P., Frebel A., Ezzeddine R., Casey A. R., 2016, *ApJ*, **832**, L3
- Ji A. P., Simon J. D., Frebel A., Venn K. A., Hansen T. T., 2019, *ApJ*, **870**, 83
- Johnston K. V., Bullock J. S., Sharma S., Font A., Robertson B. E., Leitner S. N., 2008, *ApJ*, **689**, 936
- Jönsson H., et al., 2020, *AJ*, **160**, 120
- Karlsson T., Bromm V., Bland-Hawthorn J., 2013, *Reviews of Modern Physics*, **85**, 809
- Kielty C. L., et al., 2021, *MNRAS*, **506**, 1438
- Koch A., McWilliam A., Grebel E. K., Zucker D. B., Belokurov V., 2008, *ApJ*, **688**, L13
- Koch A., Feltzing S., Adén D., Matteucci F., 2013, *A&A*, **554**, A5
- Koch A., McWilliam A., Preston G. W., Thompson I. B., 2016, *A&A*, **587**, A124
- Labrie K., Anderson K., Cárdenes R., Simpson C., Turner J. E. H., 2019, in Teuben P. J., Pound M. W., Thomas B. A., Warner E. M., eds, *Astronomical Society of the Pacific Conference Series Vol. 523, Astronomical Data Analysis Software and Systems XXVII*. p. 321
- Lamb M., et al., 2017, *MNRAS*, **465**, 3536
- Limongi M., Chieffi A., 2018, *ApJS*, **237**, 13
- Lind K., Bergemann M., Asplund M., 2012, *MNRAS*, **427**, 50
- Lucchesi R., et al., 2022, *MNRAS*, **511**, 1004
- Lucey M., et al., 2019, *MNRAS*, **488**, 2283
- Lucey M., et al., 2021, *MNRAS*, **501**, 5981
- Lucey M., et al., 2022, *MNRAS*, **509**, 122
- Mardini M. K., Frebel A., Chiti A., Meiron Y., Brauer K. V., Ou X., 2022, *ApJ*, **936**, 78
- Marigo P., Girardi L., Bressan A., Groenewegen M. A. T., Silva L., Granato G. L., 2008, *A&A*, **482**, 883
- Martin N. F., et al., 2022, *Nature*, **601**, 45
- Mashonkina L. I., Belyaev A. K., 2019, *Astronomy Letters*, **45**, 341
- Mashonkina L., Jablonka P., Pakhomov Y., Sitnova T., North P., 2017a, *A&A*, **604**, A129
- Mashonkina L., Jablonka P., Sitnova T., Pakhomov Y., North P., 2017b, *A&A*, **608**, A89
- Mashonkina L., et al., 2023, *MNRAS*, **523**, 2111
- McConnachie A. W., et al., 2022, in Evans C. J., Bryant J. J., Motohara K., eds, *Society of Photo-Optical Instrumentation Engineers (SPIE) Conference Series Vol. 12184, Ground-based and Airborne Instrumentation for Astronomy IX*. p. 121841E, doi:10.1117/12.2630407
- Mucciarelli A., Bellazzini M., Massari D., 2021, *A&A*, **653**, A90
- Ness M., et al., 2013a, *MNRAS*, **430**, 836
- Ness M., et al., 2013b, *MNRAS*, **432**, 2092
- Ness M., Debattista V. P., Bensby T., Feltzing S., Roškar R., Cole D. R., Johnson J. A., Freeman K., 2014, *ApJ*, **787**, L19
- Norris J. E., Wyse R. F. G., Gilmore G., Yong D., Frebel A., Wilkinson M. I., Belokurov V., Zucker D. B., 2010, *ApJ*, **723**, 1632
- Pazder J., Fournier P., Pawluczyk R., van Kooten M., 2014, in Navarro R., Cunningham C. R., Barto A. A., eds, *Society of Photo-Optical Instrumentation Engineers (SPIE) Conference Series Vol. 9151, Advances in Optical and Mechanical Technologies for Telescopes and Instrumentation*. p. 915124, doi:10.1117/12.2057327
- Pazder J., et al., 2020, in *Society of Photo-Optical Instrumentation Engineers (SPIE) Conference Series*. p. 1144743, doi:10.1117/12.2561985
- Pignatari M., Gallino R., Meynet G., Hirschi R., Herwig F., Wiescher M., 2008, *ApJ*, **687**, L95
- Placco V. M., Sneden C., Roederer I. U., Lawler J. E., Den Hartog E. A., Hejazi N., Maas Z., Bernath P., 2021, *Research Notes of the American Astronomical Society*, **5**, 92
- Plez B., 2012, *Turbospectrum: Code for spectral synthesis* (ascl:1205.004)
- Reggiani H., Schlafman K. C., Casey A. R., Ji A. P., 2020, *AJ*, **160**, 173
- Reichert M., Hansen C. J., Hanke M., Skúlafóttir Á., Arcones A., Grebel E. K., 2020, *A&A*, **641**, A127

- Roederer I. U., 2017, *ApJ*, **835**, 23
- Salvadori S., Bonifacio P., Caffau E., Korotin S., Andreevsky S., Spite M., Skúladóttir Á., 2019, *MNRAS*, **487**, 4261
- Santistevan I. B., Wetzel A., Sanderson R. E., El-Badry K., Samuel J., Faucher-Giguère C.-A., 2021, *MNRAS*, **505**, 921
- Schiavon R. P., et al., 2017, *MNRAS*, **466**, 1010
- Schlaufman K. C., Casey A. R., 2014, *ApJ*, **797**, 13
- Schultheis M., Rich R. M., Origlia L., Ryde N., Nandakumar G., Thorsbro B., Neumayer N., 2019, *A&A*, **627**, A152
- Schultz G. V., Wiemer W., 1975, *A&A*, **43**, 133
- Sestito F., et al., 2019, *MNRAS*, **484**, 2166
- Sestito F., et al., 2020, *MNRAS*, **497**, L7
- Sestito F., et al., 2021, *MNRAS*, **500**, 3750
- Sestito F., et al., 2023a, *arXiv e-prints*, p. [arXiv:2301.13214](#)
- Sestito F., et al., 2023b, *MNRAS*, **518**, 4557
- Sitnova T. M., et al., 2021, *MNRAS*, **504**, 1183
- Snedden C. A., 1973, PhD thesis, THE UNIVERSITY OF TEXAS AT AUSTIN.
- Sobeck J. S., et al., 2011, *AJ*, **141**, 175
- Starkenburg E., Oman K. A., Navarro J. F., Crain R. A., Fattahi A., Frenk C. S., Sawala T., Schaye J., 2017a, *MNRAS*, **465**, 2212
- Starkenburg E., et al., 2017b, *MNRAS*, **471**, 2587
- Stetson P. B., Pancino E., 2008, *PASP*, **120**, 1332
- Suda T., et al., 2008, *PASJ*, **60**, 1159
- Takahashi K., Yoshida T., Umeda H., 2018, *ApJ*, **857**, 111
- Taylor M. B., 2005, in Shopbell P., Britton M., Ebert R., eds, *Astronomical Society of the Pacific Conference Series Vol. 347, Astronomical Data Analysis Software and Systems XIV*. p. 29
- Tissera P. B., White S. D. M., Scannapieco C., 2012, *MNRAS*, **420**, 255
- Tumlinson J., 2010, *The Astrophysical Journal*, **708**, 1398
- Venn K. A., Irwin M., Shetrone M. D., Tout C. A., Hill V., Tolstoy E., 2004, *AJ*, **128**, 1177
- Venn K. A., et al., 2012, *ApJ*, **751**, 102
- Venn K. A., et al., 2020, *MNRAS*, **492**, 3241
- Vitali S., et al., 2022, *MNRAS*, **517**, 6121
- Waller F., et al., 2023, *MNRAS*, **519**, 1349
- Wenger M., et al., 2000, *A&AS*, **143**, 9
- White S. D. M., Springel V., 2000, in Weiss A., Abel T. G., Hill V., eds, *The First Stars*. p. 327 ([arXiv:astro-ph/9911378](#)), [doi:10.1007/10719504_62](#)
- Wise J. H., Turk M. J., Norman M. L., Abel T., 2012, *ApJ*, **745**, 50
- Wolf C., et al., 2018, *Publ. Astron. Soc. Australia*, **35**, e010
- Youakim K., et al., 2017, *MNRAS*, **472**, 2963

This paper has been typeset from a \LaTeX file prepared by the author.